Fortnightly Variation in the Bottom Thermal Front and Associated Circulation in a Semienclosed Sea

XIAOJIE YU, XINYU GUO, AND HIDETAKA TAKEOKA

Center for Marine Environmental Study, Ehime University, Matsuyama, Ehime, Japan

ABSTRACT

Summer hydrographic data from 1971 to 2000 demonstrate the presence of bottom cold water (BCW) and a bottom thermal front around the BCW in a semienclosed sea in the Seto Inland Sea of Japan. The horizontal gradient of water temperature across the bottom front was larger in neap tide than in spring tide, which is the opposite the pattern observed in the fortnightly variations in other areas (e.g., the Irish Sea). A numerical model for the Inland Sea reproduced the presence of BCW and a bottom front as well as the same fortnightly variation in the horizontal gradient of water temperature across the bottom front as in observational data. Being the same BCW as those in other areas, the presence of BCW in the Inland Sea is also caused by spatial variation in tidal mixing. The intensification of the bottom front in neap tide in the Inland Sea results from a combination of tidal mixing and horizontal advection of warm water to the BCW. The presence of a bottom residual current in the direction across the bottom front results in the horizontal advection of warm water to the BCW, and its fortnightly variation is responsible for the fortnightly variation of the bottom front in the Inland Sea. The presence of the BCW induces a surface cyclonic circulation in the direction approximately along the bottom front; the intensification and weakening of the bottom front with the spring–neap tidal cycle, combined with the fortnightly variation in the bottom boundary layer thickness, produce a slightly stronger surface cyclonic circulation in neap tide than in spring tide.

1. Introduction

Following the study by Simpson and Hunter (1974) that revealed the presence of a tidal front in the Irish Sea and its formation mechanism, there have been many studies on surface thermal fronts, that is, tidal fronts in shelf seas and bays in summer (e.g., Simpson et al. 1978; Ou 1984; Loder and Greenberg 1986; Lie 1989; Wang et al. 1990; Simpson and Sharples 1994). Spatial variations in tidal currents induce the establishment of mixed regions and stratified areas. Strong tidal currents in mixed regions overcome the buoyancy input by surface heat fluxes and maintain homogeneity in the water column; weak tidal currents in areas of stratification, however, cannot homogenize the water column in the vertical direction. The transition zone between these two regions is the tidal front, across which the surface temperature gradient is large.

The thermal front is present not only in the surface layer but also in the bottom layer. Water is usually colder in the bottom layer of a stratified area compared to in mixed areas and is called bottom cold water (BCW). Consequently, the bottom thermal front, although not as demarcated as the surface one, forms between the mixed area and the stratified area. The presence of BCW and the bottom front are confirmed by field observations in the Irish Sea (Hill et al. 1997; Horsburgh et al. 2000; Xing and Davies 2001b; Brown et al. 2003), North Sea (Brown et al. 1999), and Yellow Sea (Yuan and Li 1993; Su and Huang 1995).

Some studies have reported residual currents around the bottom thermal front and BCW. Based on observations, Hill et al. (1994) reported the presence of a cyclonic gyre in the western Irish Sea in summer and concluded that the gyre is closely associated with the bottom thermal front and the BCW. Using the observed density field and the thermal-wind equation, Horsburgh et al. (2000) predicted a cyclonic, near-surface jet along the bottom thermal front in the Irish Sea in summer. Using the same method, Hill et al. (2008) demonstrated that a density field associated with a bottom thermal front can be used to diagnose a surface current that is

Corresponding author address: Xinyu Guo, Center for Marine Environmental Studies, Ehime University, 2-5 Bunkyo-Cho, Matsuyama 790-8577, Japan.
E-mail: guoxinyu@sci.ehime-u.ac.jp
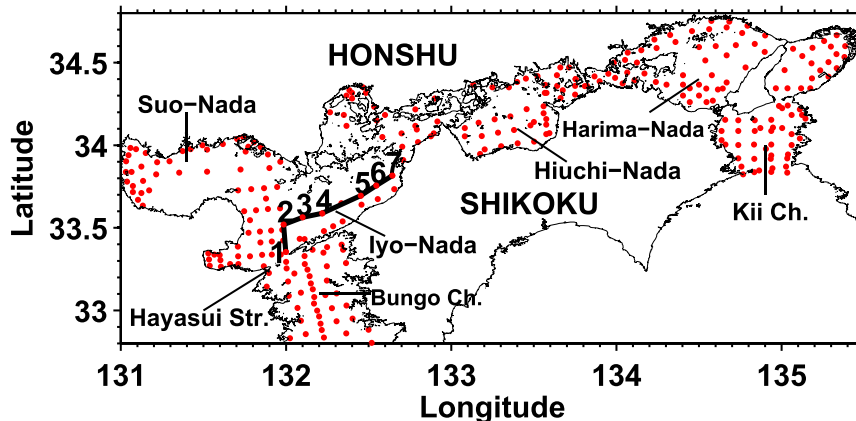
FIG. 1. Monthly sampling stations (red dots) in the Seto Inland Sea. The black line with numbers from 1 to 7 denotes stations bisecting the BCW from which data are presented in Fig. 5.

consistent with the movement of drifters. Bottom friction is likely an essential condition for the formation of surface cyclonic circulation (Hill 1996). Three-dimensional models developed based on realistic bathymetry data and forcing inputs were also used to reproduce the BCW and to develop interpretation of its dynamics (Xing and Davies 2001b; Horsburgh and Hill 2003; Holt and Proctor 2003; Xing and Davies 2005; Davies and Xing 2006).

Since the tidal current cycles between spring tide and neap tide, its induced vertical mixing must also have the same cycle. A general hypothesis on this variation is that the mixed area becomes enlarged during spring tide when the position of the tidal front shifts to the stratified area; the mixed area becomes small in neap tide, and the tidal front retreats to the mixed area (Simpson and Bowers 1981; Mountain and Taylor 1996). Yanagi and Tamaru (1990) and Sun and Isobe (2006) reported fortnightly variation not only in the position of the tidal front but also in the horizontal gradient of the sea surface temperature across the tidal front that is intensified in spring tide and weakened in neap tide. Based on field measurements, Lwiza et al. (1991) found that the residual current along a tidal front in the North Sea is strong in spring tide and weak in neap tide.

Based on the same principle, the bottom thermal front and associated circulation are also affected by fortnightly variation in the tidal current. Using a numerical model, Horsburgh and Hill (2003) found that the horizontal gradient of bottom temperature across the bottom thermal front and the kinetic energy of the residual current above the bottom thermal front become stronger after spring tide but weaker after neap tide in the Irish Sea. Using a different numerical model, Luyten et al. (2003) also demonstrated fortnightly variation in the vertical structure of water temperature and thermal circulation in the North Sea: the surface mixed layer

becomes shallow (deep) and the baroclinic circulation is intensified (weakened) during spring (neap) tide.

The nature of the surface tidal front and the bottom thermal front is such that they form not only in shelf seas but also in bays and inland seas where the change in tidal current is as large as in the shelf seas. The Seto Inland Sea (Fig. 1) is a semienclosed sea located in western Japan. It opens to the Pacific Ocean through the Bungo
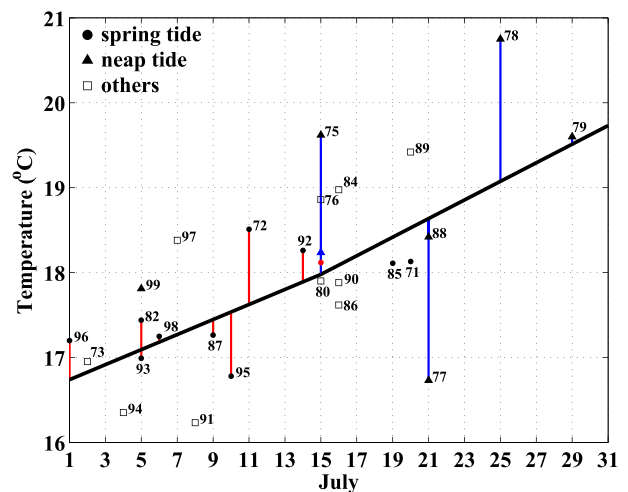
FIG. 2. Observational data in July during 1971 to 2000 in Iyo-nada grouped as spring tide (circles), neap tide (triangles), and others (squares). Abscissa is the observational month (July) and day. Numbers inside the panel denote the observational year. Water temperature (°C) is that at 50-m depth for station 3. The black line shows seasonal variation given by monthly climatology in June, July, and August, defined at the middle of each month. The circles with red lines (72, 82, 87, 92, 93, 95, 96, and 98) denote the data averaged for spring tide, and the averaged result is shown by a red circle on 15 Jul. The triangles with blue lines (75, 77, 78, 79, and 88) indicate the data averaged for neap tide, and the averaged result is shown with a blue triangle on 15 Jul.
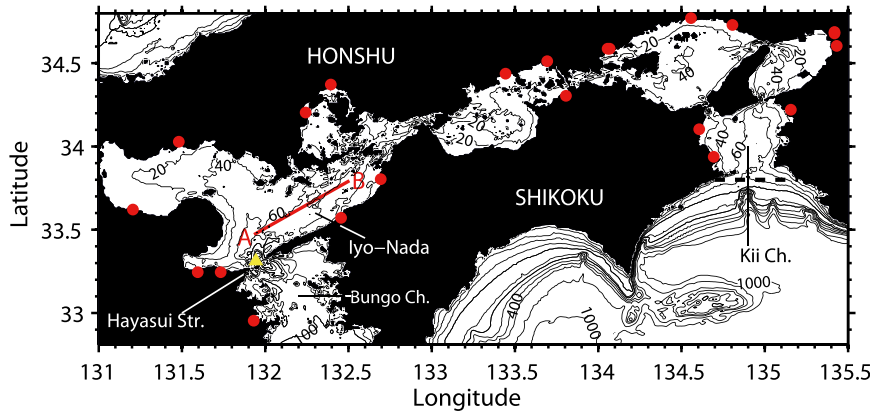
FIG. 3. Bathymetry (m) and model domain of the Seto Inland Sea. The open boundaries are the south sides of the Bungo Channel (south boundary) and Kii Channel (dashed line). The red dots along the coastline denote the mouths of rivers. Section AB in the model is denoted as a red line. The yellow triangle in the Hayasui Strait indicates the measurement point for tide elevation and tidal current (Fig. 7).

Channel and Kii Channel, through which the tidal wave enters the Seto Inland Sea (Yanagi and Higuchi 1981). Inside the Seto Inland Sea, there are several wide basins called ''nada'' in Japanese, including Iyo-nada, Suo-nada, Hiuchi-nada, and Harima-nada, which are interconnected by narrow straits. The tidal currents are strong ($>1\,\mathrm{m\,s}^{-1}$) in the straits due to the small cross-sectional area but weak ($\sim 0.1\,\mathrm{m\,s}^{-1}$) in the nadas due to their large cross-sectional area (Takeoka 2002).

Different tidal mixing capability between the straits and the nadas results in different vertical density structure in summer between the two areas. Water in the straits is well mixed and the water temperature increases from spring to summer simultaneously within the entire water column. On the other hand, water in the nadas is warmed quickly in the surface layer and slowly in the bottom layer; consequently strong stratification develops in summer (Takeoka 1985). The tidal fronts, which have apparent fortnightly variation, are formed in the surface layer between the well-mixed straits and the stratified nadas (Yanagi and Tamaru 1990).

Another aspect of different tidal mixing in straits and nadas is that the coldest water is found in the bottom layer of the nadas in summer because stratification there inhibits downward heat transfer (Takeoka 1985). Although not as sharp as the surface tidal front, a bottom thermal front can be identified around the coldest water in summer (Takeoka et al. 1993). The presence of the BCWs has been suggested to be a key factor of the formation of subsurface chlorophyll-a maximum above and around the BCWs because of the supply of nutrients from the BCW to the area with high chlorophyll-a concentration (Yamamoto et al. 2000). The subtidal current above the BCW shows surface cyclonic circulation such as that in the

Hiuchi-nada (Guo et al. 2004), Iyo-nada, Suo-nada, and Harima-nada (Chang et al. 2009). However, its fortnightly variation remains largely unknown.

To date, fortnightly variation in the bottom thermal front and associated circulation have been examined by two numerical simulations (Horsburgh and Hill 2003; Luyten et al. 2003), but examination of fortnightly variation based on observational data remains lacking. Furthermore, there is likely different fortnightly variation in the bottom thermal front between the inland sea and the shelf sea (e.g., the Irish Sea). As our first objective in this study, we want to confirm the fortnightly variation in the bottom thermal front using observational data. We collected in situ hydrographic data in the Seto Inland Sea from 1971 to 2000 from the Fishery Research Agency, Japan, and examined fortnightly variation of the water temperature gradient across the bottom of the front in summer. Our analysis of the hydrographic data presents a strong bottom thermal front in neap tide rather than in spring tide, which is the opposite of the fortnightly variations identified by the numerical models for the Irish Sea (Horsburgh and Hill 2003).

The second objective in this study is to understand why the unexpected fortnightly variation in the bottom thermal front occurs in the Seto Inland Sea and how it

TABLE 1. Model cases and forcing factors.

Case 0	Case 1	Case 2	Case 3	Case 4
Tide	Tide	Tide	Tide	Tide
Heating		Heating	Heating	Heating
River discharge			River discharge	Winds
Winds				
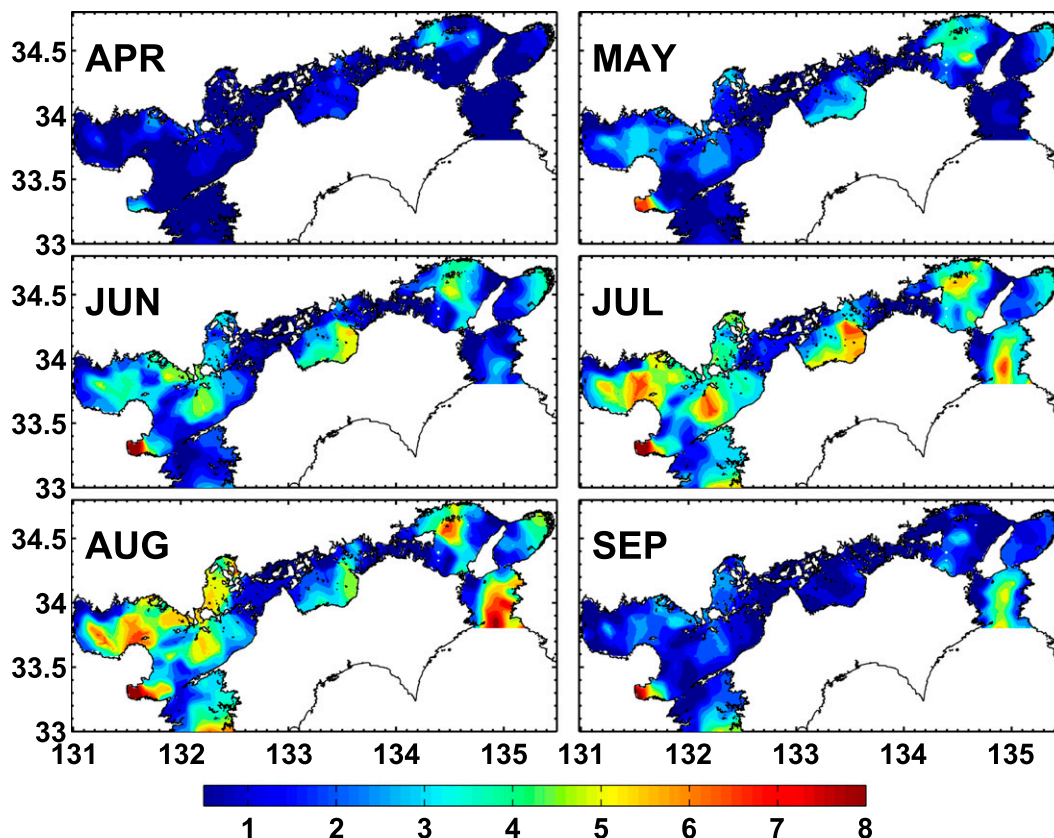
FIG. 4. Difference in water temperature (°C) between the surface layer (0 m) and bottom layer (the deepest sampling depth at each station) in the climatology data from April to September, obtained as averages of data collected in the same months between 1971 to 2000.

affects the fortnightly variation in the circulation above the bottom thermal front. To reach this goal, we developed a three-dimensional numerical model that can reproduce the presence of the BCW in the Seto Inland Sea and the fortnightly variation in the bottom thermal front found in the observational data.

2. Observational data and model description

Regular hydrographic observations at monthly intervals have been carried out over the past 40 yr by prefectural fishery research centers at 344 stations in the Seto Inland Sea (Fig. 1), and we were able to obtain data from 1971 to 2000, including water temperature and salinity at depths of 0, 10, 20, 30, 50, 75, and 100 m.

The data were processed as follows: To determine monthly climatology and to reveal seasonal variation, we averaged data collected in the same month over 30 yr (1971–2000). As shown later, the bottom thermal front was well developed in summer (June–August). July was selected as the best month for examining fortnightly variations based on June being the rainy season and

August being the typhoon season in the Seto Inland Sea. Among several areas of BCW in the Seto Inland Sea, we concentrated on those in the Iyo-nada having a water depth of approximately 70 m, close to that in the Irish Sea.

For data analysis based on tides (fortnightly variation), we calculated the moon age from the observational day of every data and chose 5 days centered on the day of spring (neap) tide as the period for analyzing data from the same spring (neap) tide. For the BCW in the Iyo-nada, we chose seven stations (1–7 in Fig. 1) where the observations were finished in the same day. During a period from 1971 to 2000, there were eight observations whose moon age were spring tide and whose Julian calendar were in the first half of July and five observations whose moon age were neap tide and whose Julian calendar were in second half of July (Fig. 2). We defined the former eight observations as the group for spring tide and the latter five observations as the group for neap tide. To avoid influences of seasonal variation on fortnightly variation, we calculated the anomaly of each set of data to its corresponding seasonal signal and averaged all the anomalies in each
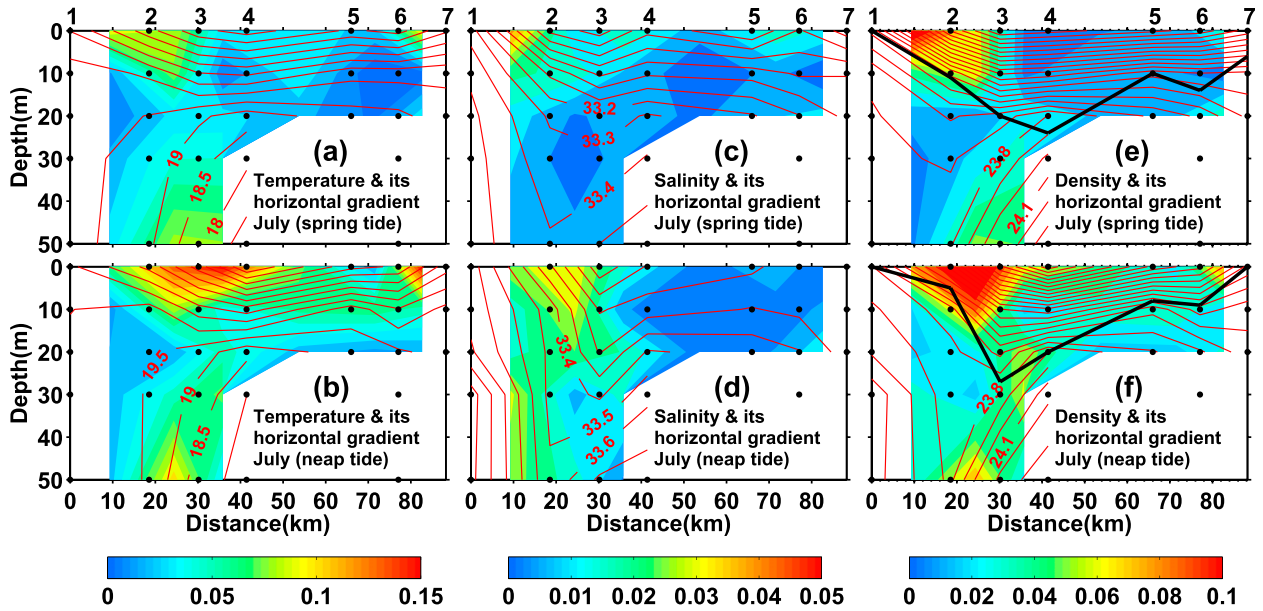
FIG. 5. Depths (m) of data (black dots), contours (red lines), and magnitude of the horizontal gradient (color) along the sampling stations bisecting the BCW (stations 1 through 7 in Fig. 1). (a),(b) Water temperature (°C); (c),(d) salinity; and (e),(f) density (kg m^{-3}). The units for gradient are °C km^{-1} for water temperature, km^{-1} for salinity, and kg m^{-3} km^{-1} for density. The upper three panels show the spring tide period, and the lower three panels show the neap tide period. The thick black lines in (e) and (f) denote the position of the bottom boundary layer where the density is 0.5 kg m^{-3} less than that at the deepest data point.

group to represent fortnightly variation. The seasonal signal corresponding to each set of data was calculated by substituting the observational date to a seasonal variation curve given by the monthly climatology that is the average of all the data in the same month from 1971 to 2000 and is defined at the middle of each month (black thick line in Fig. 2). To obtain a visual effect close to a field observation, we finally added the seasonal signal on 15 July to the averaged anomaly for the spring tide and neap tide groups, respectively.

The model was applied to the area of the Seto Inland Sea shown along with the bathymetry in Fig. 3. The numerical model of Chang et al. (2009) was used in this study without modification. The model is based on the Princeton Ocean Model, which is a three-dimensional, primitive equation, sigma-coordinate model (Blumberg and Mellor 1987; Mellor 2003). It uses a second momentum turbulent closure scheme to calculate the vertical mixing coefficients (Mellor and Yamada 1982) and the Smagorinsky formulation to parameterize the horizontal mixing coefficients (Smagorinsky 1963).

The model has a spatial resolution of ~1 km (1/120° in the meridional direction and 1/80° in the zonal direction) and 21 sigma layers in the vertical direction. The forcing includes wind stresses, heat flux, evaporation and precipitation, and river discharges, all of which are specified in the model using monthly climatology data (Chang et al. 2009) for the purpose of reproducing

seasonal variations. Along the open boundary, monthly mean water temperature and salinity values and the monthly normal component of subtidal velocity and surface elevation are specified from a diagnostic model with a larger domain. Tidal currents represented by the sum of four tidal constituents, M_2, S_2, K_1, and O_1, having harmonic constants from a tide model for a larger domain (Guo et al. 2013), were linearly superimposed on the corresponding normal component of the subtidal velocity at the open boundary.

The model calculation was started in January with a total integration period of 3 yr. The model results were saved at 1-h intervals. A tide filter (Hanawa and Mitsudera 1985) was used to remove the tidal components; the current without the tidal component is called a residual current in this study. A stationary seasonal variation was confirmed by comparing the model results in the second and third years of model integration. The analysis was based on model results in the third year. The settings of the model were divided into five cases with different considerations of forcing factors (Table 1): case 0, all forcing factors were considered, including the tide, surface heat flux, river discharge and wind; case 1, only tide was considered; case 2, tide and surface heat flux were considered; case 3, tide, surface heat flux, and river discharge were considered; and case 4, tide, surface heat flux, and wind were considered.
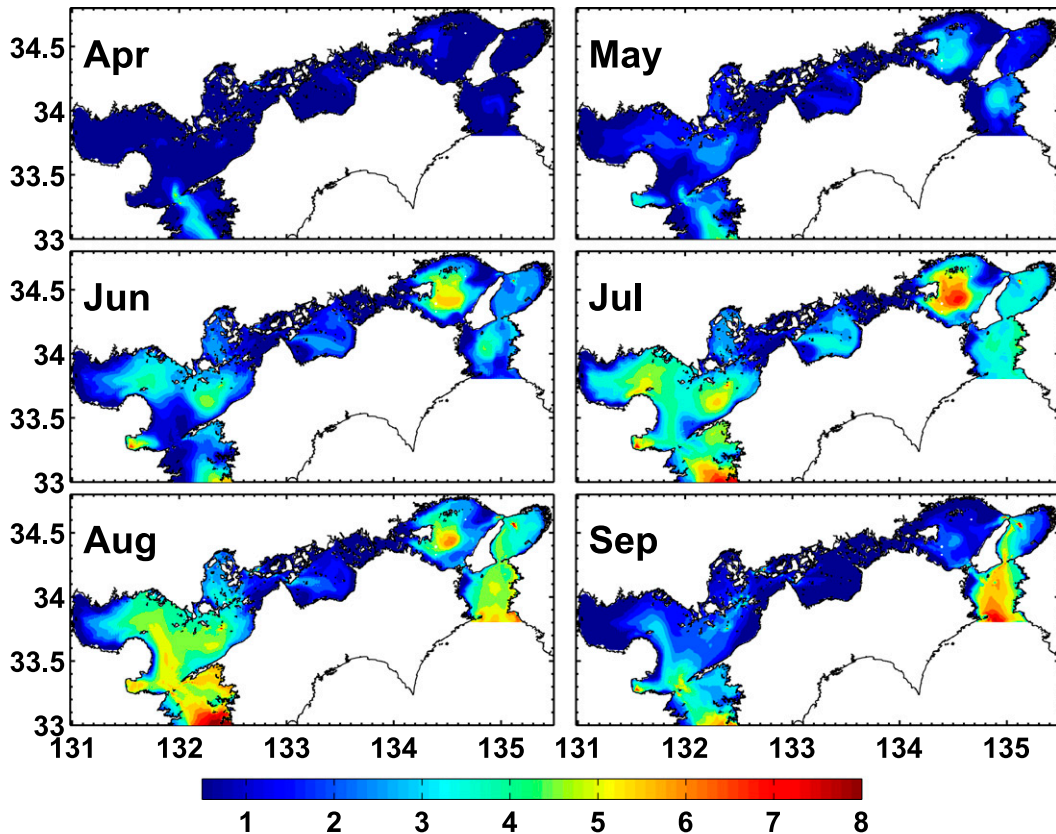
FIG. 6. Difference of monthly averaged water temperature (°C) between the surface layer (0 m) and bottom layer (the deepest grid point) from April to September (case 0).

3. Results

a. Observational data

We used the difference in water temperature between the surface layer (0 m) and the bottom layer (the deepest sampling depth at each station) to demonstrate the development of seasonal stratification in the Seto Inland Sea from April to September (Fig. 4). Temperature differences began to appear in April, increased from May to June, reached a maximum in July and August,
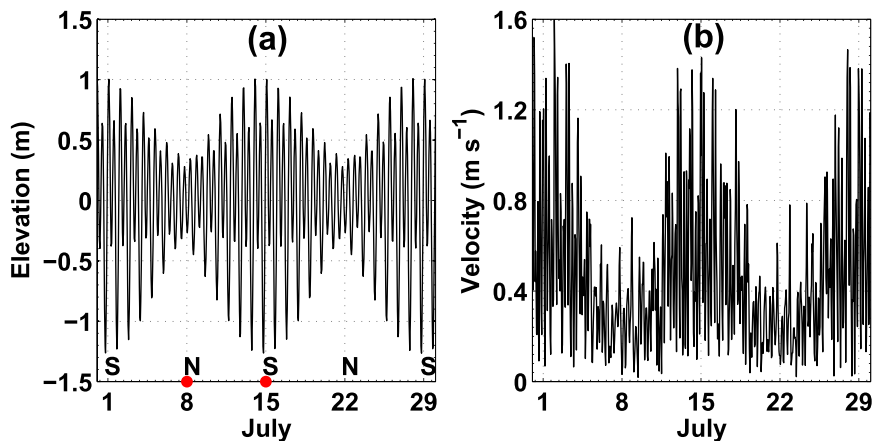
FIG. 7. (a) Tide elevation (m) and (b) tidal current velocity (m s^{-1}) in the Hayasui Strait (yellow triangle in Fig. 3) in case 1. In (a), S indicates spring tide and N indicates neap tide. The red dots in (a) indicate the day corresponding to spring and neap tides, on which the model results are presented in the following figures.
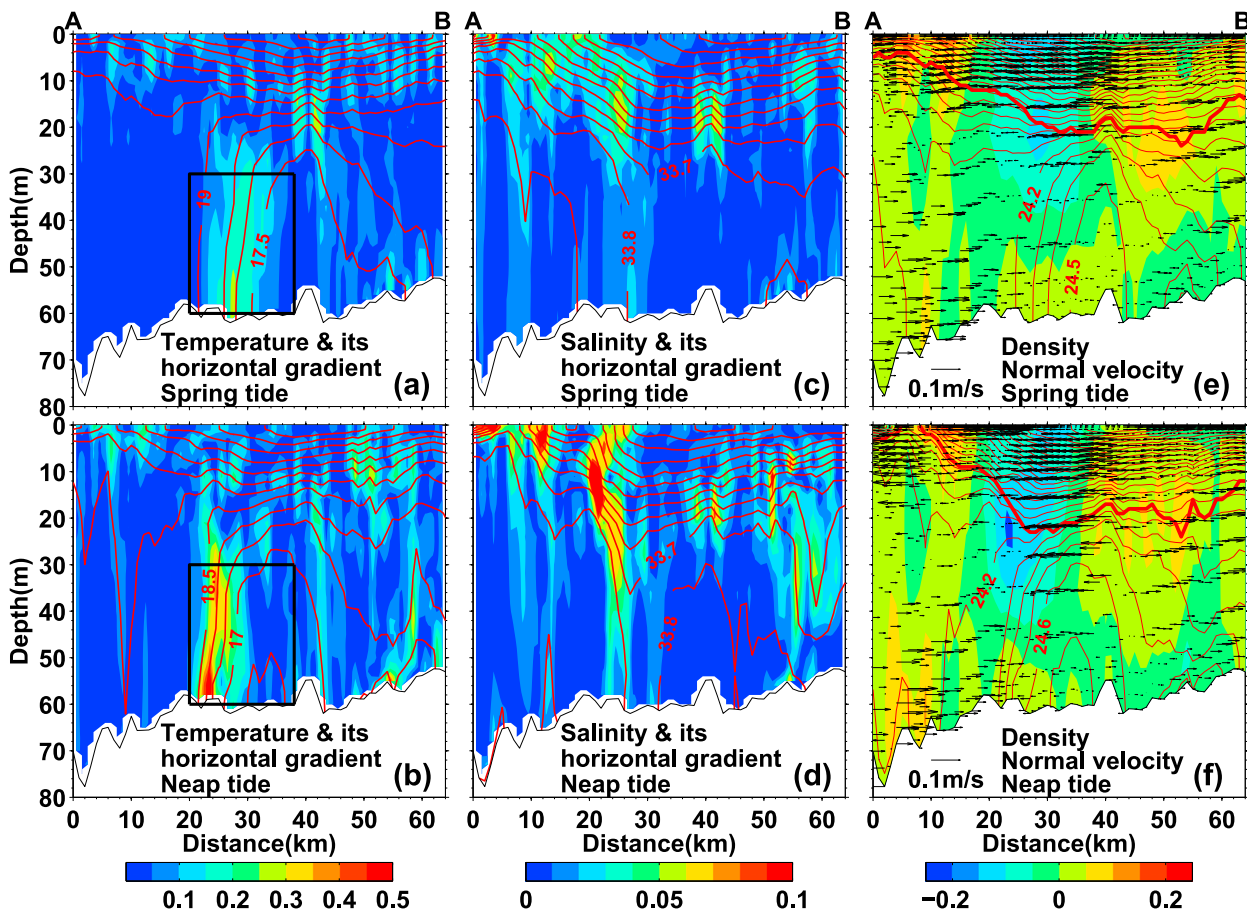
FIG. 8. Model result (red line) and magnitude of its horizontal gradient (color) along section AB. (a),(b) Water temperature (°C); (c),(d) salinity; and (e),(f) density (kg m^{-3}) for case 0. The units for gradient are °C km^{-1} for water temperature, km^{-1} for salinity, and kg m^{-3} km^{-1} for density. Color in (e) and (f) denotes the velocity (m s^{-1}) of normal residual current to section AB. Positive values indicate current flowing northwestward, while negative values indicate current flowing southeastward. Arrows in (e) and (f) indicate the residual current (m s^{-1}) along section AB. The position of section AB is shown in Fig. 3. The upper three panels show data from a day in spring tide (red S in Fig. 7), and the lower three panels show data from a day in neap tide (red N in Fig. 7). The thick red lines in (e) and (f) denote the position of the bottom boundary layer where the density is 0.5 kg m^{-3} less than that of the bottom grid point. The black boxes in (a) and (b) show the area where the maximum bottom temperature gradient is, as shown in Fig. 10a.

and disappeared in September. Along with seasonal variation, there was also apparent spatial variation: larger in the nadas and smaller in the straits. The areas with the largest differences in water temperature in the nadas in July corresponded to areas of BCW.

Along the stations bisecting the BCW in the Iyo-nada (labeled 1–7 on the black line in Fig. 1), the lowest water temperature was found at a depth of 50 m at station 4, but the highest temperature at the sea surface was observed at the same station (Figs. 5a,b). The water temperature at station 1 was generally homogeneous. Consequently, the greatest vertical difference in water temperature was at station 4 and the smallest is at station 1. This spatial structure is maintained at both spring tide and neap tide (Figs. 5a,b). Salinity was generally low in the surface layer but was higher in the bottom layer

(Figs. 5c,d). The influence of salinity on the spatial structure of the density field was slight, and the spatial variations in the density field were essentially determined by water temperature (Figs. 5e,f).

The fortnightly variation in temperature, salinity, and density shown in Fig. 5 illustrates that the greatest variation is found mainly in the horizontal gradients in the bottom water for temperature and density, which were smaller in spring tide (Figs. 5a,e) than in neap tide (Figs. 5b,f). The maximum horizontal gradient of bottom water temperature was ~0.07°C km^{-1} in spring tide (Fig. 5a) and ~0.09°C km^{-1} in neap tide (Fig. 5b), increasing by ~0.02°C km^{-1} from spring tide to neap tide. The bottom thermal front defined as the place with the maximum horizontal gradient of water temperature was located between stations 2 and 3, and its position
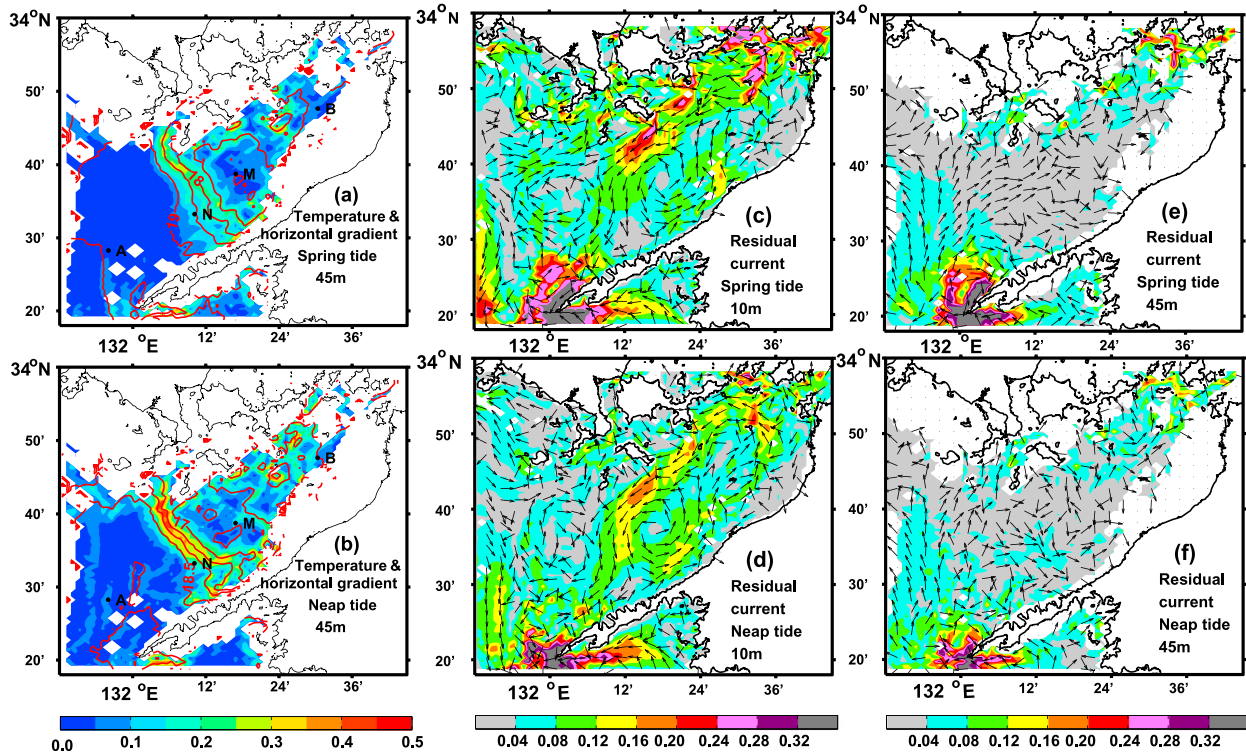
FIG. 9. (a) Horizontal distribution of water temperature (°C; red line) and the magnitude of the gradient (°C km^{-1}; color) at a depth of 45 m in spring tide; (b) as in (a), but for neap tide; residual currents (m s^{-1}) at depths of (c) 10 m and (e) 45 m for spring tide; residual currents (m s^{-1}) at depths of (d)10 m and (f) 45 m for neap tide. All results are from case 0. The arrows in (c)–(f) show the direction of the current, while the color indicates the magnitude of current.

changed little with the spring–neap tidal cycle. The fortnightly variation in the horizontal gradient of bottom water temperature here is the opposite of the pattern observed in the Irish Sea where the horizontal gradient of bottom water temperature is larger in spring tide than in neap tide (Horsburgh and Hill 2003).

b. Model results

The horizontal distribution of water temperature differences between the surface layer (0 m) and bottom layer (the deepest depth on each model grid) in the model results shows that stratification in the nadas starts in April, increases in May and June, becomes strongest in July and August, and gradually decreases in September (Fig. 6). This progression is consistent with the observational data (Fig. 4).

The enclosed structure of water temperature difference between the surface layer and bottom layer, corresponding to the presence of BCW, is also found in the model results. By comparing the location of BCWs (Figs. 4, 6) with the distribution of the Simpson–Hunter parameter $\log_{10}(H/U^3)$ (Fig. 4 in Takeoka 2002; H is water depth; U is amplitude of tidal currents) or that estimated by using our model results (data not shown), it is

apparent that the BCWs approximately overlap with areas with a large value of $\log_{10}(H/U^3)$ where the tidal mixing is weak. This fact suggests that the spatial variation of tidal mixing is an essential condition for the formation and location of BCW and bottom thermal front.

1) FORTNIGHTLY VARIATION OF HORIZONTAL GRADIENT OF BOTTOM WATER TEMPERATURE IN IYO-NADA

From the time series of tide elevation (Fig. 7a) and tidal current velocity (Fig. 7b) at the Hayasui Strait (indicated by a yellow triangle in Fig. 3) in July based on the results of a model driven by tide forcing alone (case 1), we can see that there are three spring tides (1, 15, and 29 July) and two neap tides (8 and 22 July). The tide elevation ranged from about −1.5 to 1 m in spring tide and from −0.5 to 0.5 m in neap tide. The tidal current was about 1.5 m s^{-1} in spring tide and 0.4 m s^{-1} in neap tide. For a purpose of examining fortnightly variations in the bottom thermal front and associated residual currents, we mainly analyzed the results on 8 July (neap tide) and 15 July (spring tide).

The model results were similar to observational data, showing a general spatial distribution of water
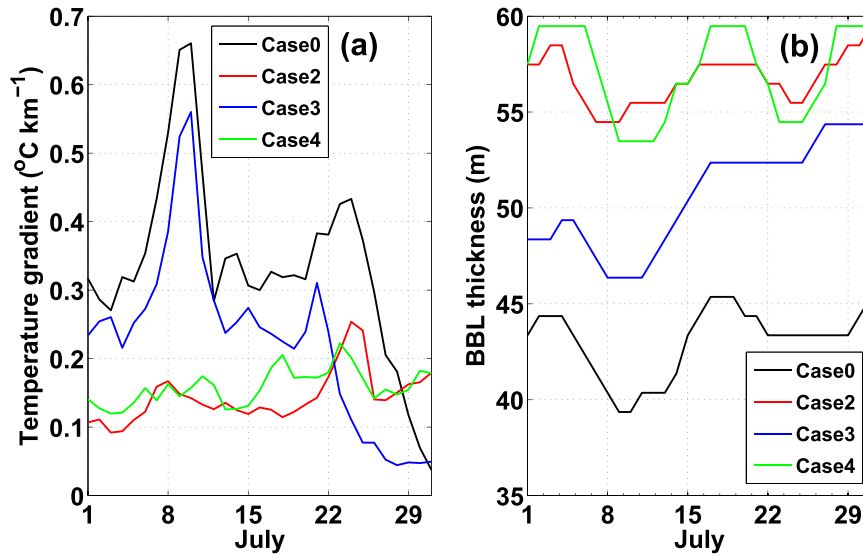
FIG. 10. (a) Time series of the maximum value of the water temperature gradient (°C km^{-1}) within the area of the black box in Fig. 8a for each of the four cases. (b) Time series of BBL thickness (m; red thick line in Fig. 8e) at the location with maximum water temperature gradient shown in (a) for four cases.

temperature across the BCW in the Iyo-nada that does not change with the modulation of spring and neap tides (Figs. 8a,b). The fortnightly variation appears mostly in the horizontal gradient of bottom water temperature that is larger in neap tide than in spring tide by about 0.25°C km^{-1} (Figs. 8a,b). The pattern of salinity in the model results (Figs. 8c,d) was similar to that in the observational data, being low in the surface layer and high in the bottom layer. The bottom layer density generally follows the water temperature, and its gradient is also larger in neap tide than in spring tide, inferred from the spaces among contour lines (Figs. 8e,f).

The magnitude of the horizontal temperature gradient at a depth of 45 m indicates that an increased horizontal gradient of water temperature in neap tide occurred in a large area between the Iyo-nada and the Hayasui Strait (Figs. 9a,b). The water temperatures ranged from 17.0° to 18.5°C in a narrowband in neap tide (Fig. 9b) and from 17.5° to 19.0°C in a slightly wider band in spring tide (Fig. 9a).

The time series of the maximum horizontal gradient of bottom water temperature around the bottom thermal front (area enclosed in the black box in Figs. 8a and 8b) showed a sequential modulation in July with a cycle between spring tide and neap tide (black line in Fig. 10a), which was smaller in spring tide and larger in neap tide. The magnitude had a value of ~0.35°C km^{-1} in spring tide and ~0.65°C km^{-1} in neap tide. These values are slightly larger than the observed results, but the intensification of the bottom

thermal front in neap tide is consistent with the observations.

2) FORTNIGHTLY VARIATION OF CIRCULATION IN IYO-NADA

From the vertical distribution of the residual current normal to section AB (color tone in Figs. 8e,f), we can identify three major structures. One is a generally positive surface current near the strait (x coordinate = 0–15 km). The others are from surface layer to subsurface layer: a negative current structure from 15 to 35 km and a positive current structure from 35 to 55 km. The two opposite currents are ~0.15 m s^{-1} in neap tide and ~0.10 m s^{-1} in spring tide.

The two opposite currents are a part of the cyclonic circulation above the BCW in Iyo-nada (Figs. 9c,d). This circulation is slightly stronger in neap tide than in spring tide. For example, the northeastward current on the eastern side of the cyclonic circulation was about 0.12 to 0.16 m s^{-1} in neap tide but 0.08 to 0.12 m s^{-1} in spring tide.

The residual current parallel to section AB (arrows in Figs. 8e,f) flows from the BCW to the strait in the surface layer but from the strait to the BCW in the bottom layer. The surface current parallel to section AB is likely a part of the southwestward current on western side of the cyclonic circulation above the BCW (Figs. 9c,d). After passing the area of BCW, this surface current separates from the cyclonic circulation above the BCW and flows toward the strait. The bottom current parallel to section
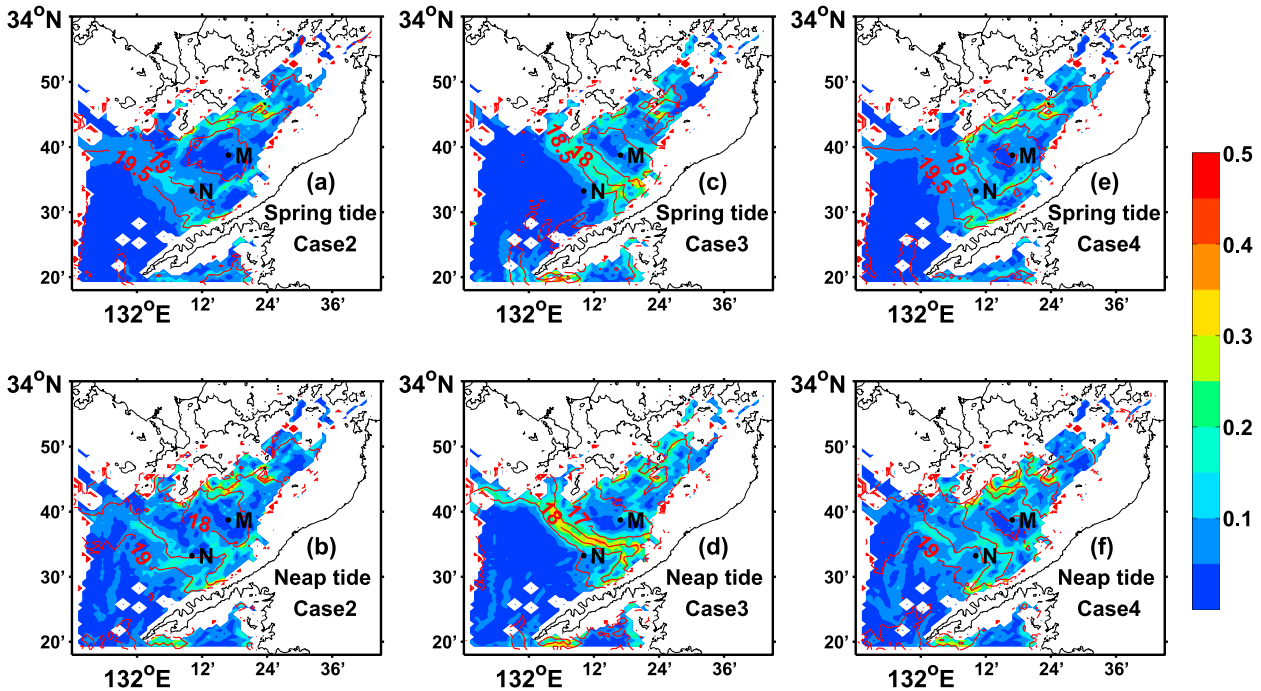
FIG. 11. Horizontal distribution of water temperature (°C; red line) and magnitude of gradient (°C km^{-1}; color overlay) at a depth of 45 m for cases 2, 3, and 4. (top) Spring tide and (bottom) neap tide.

AB is strong in the area close to the strait and weak in the area of BCW (Figs. 9e,f). Between the strait and the BCW, the bottom current is weak and does not have a fixed direction in neap tide but has a strong and fixed direction in spring tide (Figs. 9e,f). As shown in section 4a, this fortnightly variation of bottom residual current between the strait and the BCW plays an important role in the fortnightly variation of bottom thermal front.

4. Discussion

a. Causes of stronger horizontal gradient of bottom water temperature in neap tide than in spring tide

The formation of the BCW is essentially caused by surface heating and spatial variation in tidal mixing; the fortnightly variation in the BCW is therefore generally considered to be a result of the change in local mixing ability. However, other processes such as the change in ambient currents with tidal modulation can also modify the relation between the BCW and the tidal cycle. To find the dynamical causes for the intensification of the bottom horizontal gradient of water temperature in neap tide in our study area, which was confirmed by both observational data and model results, we designed three numerical experiments (Table 1) with the following forcing factors: tide and surface heat flux (case 2); tide, surface heat flux, and river discharge (case 3); and tide, surface heat flux, and wind (case 4).

The horizontal gradient of the bottom water temperature has similar temporal variation in cases 0 and 3 (Fig. 10a), indicating that wind plays a negligible role in fortnightly variation. The same implications are present for similar temporal variations of horizontal gradient of bottom water temperature in cases 2 and 4 (Fig. 10a).
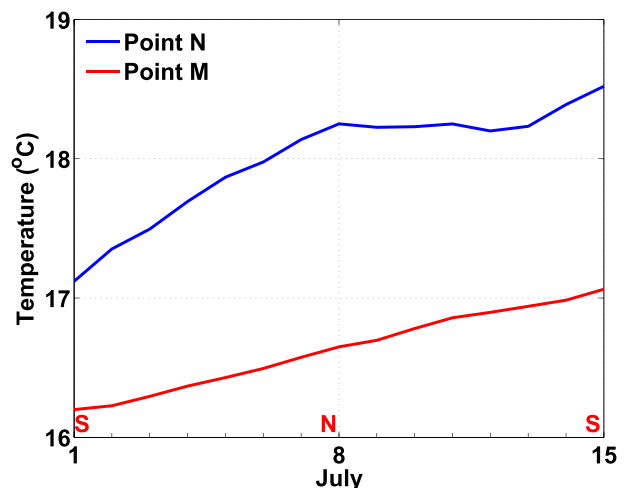
FIG. 12. Time series of water temperature (°C; after being detided by a tide filter) at grid point M (red line) and grid point N (blue line) shown on Fig. 9a at a depth of 45 m for case 0; S and N in red represent spring tide and neap tide, respectively.
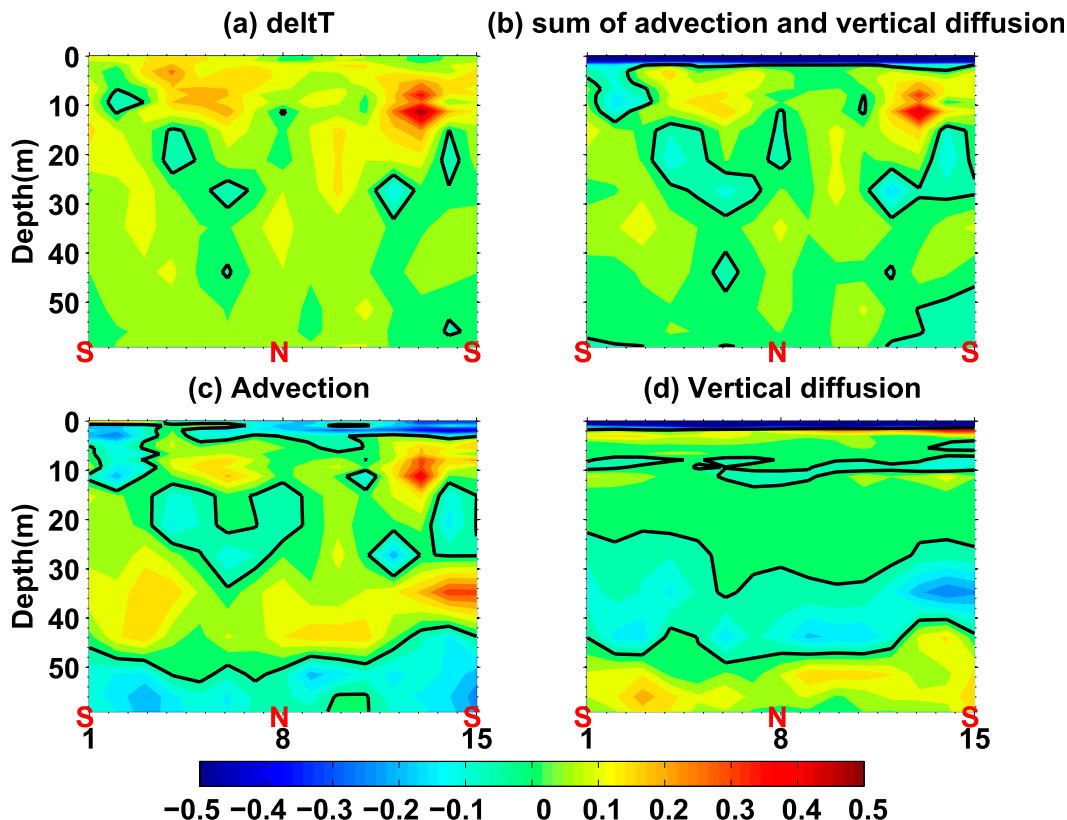
FIG. 13. (a) Daily increase in water temperature, (b) sum of advection and vertical diffusion terms, (c) advection term, (d) vertical diffusion term [contour interval (CI) = 0.05] in July at grid point M for case 0; S and N in red represent spring and neap tides, respectively (All values °C).

Case 2 shows a little stronger horizontal gradient of bottom water temperature in neap tide than in spring tide, but the magnitude of the gradient and its fortnightly variation range are much smaller than those in case 0 (Fig. 10a). Case 3 shows a similar magnitude of gradient of bottom water temperature and a similar fortnightly variation range as case 0. Therefore, river discharge is an important forcing factor for the magnitude of the bottom water temperature gradient and its fortnightly variation in our study area.

The fortnightly variations of the bottom boundary layer (BBL) in four cases (Fig. 10b) are the same: thick in spring tide and thin in neap tide, corresponding well to the change of tidal mixing. On the other hand, the BBL changes largely among four cases: thicker in cases 2 and 4 than in cases 0 and 3 and thicker in case 3 than in case 0. The addition of river discharge intensifies stratification and therefore suppresses the development of BBL in cases 0 and 3. The difference between case 0 and case 3 is the wind stresses, the inclusion of which probably intensifies surface mixing in case 0, promotes downward transport of surface water with low salinity and high temperature water, and results in a thinner BBL in case 0 than in case 3.

The horizontal distribution of water temperature and its gradient at a depth of 45 m in cases 2, 3, and 4 (Fig. 11) confirms the interpretation from Fig. 10a. Cases 2, 3, and 4 also show a larger gradient of water temperature in neap tide than in spring tide, which is the same as case 0 (Fig. 9). In cases 2 and 4, the magnitude of the temperature gradient and its fortnightly variation range are smaller than those in case 0 (Fig. 9), while in case 3 the magnitude of the temperature gradient and its fortnightly variation range becomes larger, which is close to those in case 0 (Fig. 9).

To demonstrate the critical process in the fortnightly variation described earlier, we compared the results at two grid points (M and N in Fig. 9a) in case 0. Point M is located inside the BCW, while point N is at the outer edge of the BCW. The temperature at point M increased at almost the same rate during the spring–neap–spring tidal cycle (Fig. 12). However, the temperature at point N increased much faster from spring tide to neap tide, stopped, or even decreased around neap tide and then increased to the next spring tide. Such differences in the rate of increase between points M and N induce a larger difference between these two points in neap tide than in
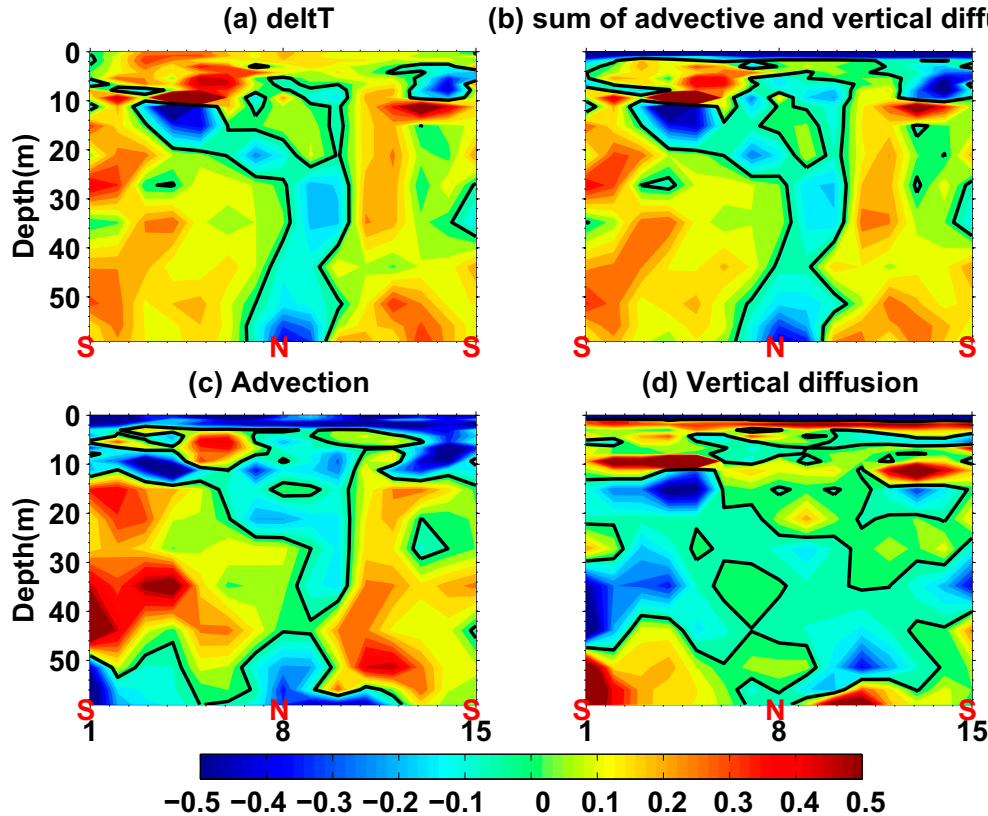
FIG. 14. As in Fig. 13, but for grid point N.

spring tide and finally generate the larger gradient in neap tide than in spring tide.

To identify an explanation for the different rate of bottom water temperature increase inside and outside the BCW, we calculated the contribution of the terms in the equation for water temperature.

The change in water temperature T over change in time t is given by

$$\frac{\overline{\partial T}}{\partial t} = \overline{\text{AdvT}} + \overline{\text{VdfT}} + \overline{\text{HdfT}} + \overline{\text{RadT}}, \quad (1)$$

where AdvT is the advection term, VdfT is the vertical diffusion term, HdfT is the horizontal diffusion term, RadT is the radiation term, and the overbar above each term is the tide filter. The daily change in water temperature can be obtained by integrating Eq. (1) over 24 h as shown in Eq. (2):

$$\Delta \overline{T}_{\text{daily}} = \int_0^{24} \overline{\text{AdvT}} \, dt + \int_0^{24} \overline{\text{VdfT}} \, dt$$
$$+ \int_0^{24} \overline{\text{HdfT}} \, dt + \int_0^{24} \overline{\text{RadT}} \, dt. \quad (2)$$

Since the horizontal diffusion term is much smaller than the advection and vertical diffusion terms, and the

radiation term does not vary with tidal cycle, we focus on the relationship between the advection and vertical diffusion terms with respect to the daily change in temperature.

The daily change of water temperature at point M (Fig. 13a) is mainly controlled by the advection and vertical diffusion terms because the sum of advection and vertical diffusion terms (Fig. 13b) may explain almost all of the variations in Fig. 13a. The advection in the midlayer is generally positive (Fig. 13c), indicating that advection brings warmer water, therefore increasing the water temperature at point M. The vertical diffusion term in the midlayer is generally negative (Fig. 13d), indicating that the heat transferred to the midlayer by advection is distributed downward through vertical diffusion. Both advection and vertical diffusion show greater values in the spring tide than in neap tide, but the sum of the two does not show apparent fortnightly variation (Fig. 13b). Consequently, the water temperature at point M increases at the same rate during the spring–neap–spring tidal cycle.

The variation of water temperature at point N (Fig. 14a) is also controlled by the advection and vertical diffusion term (Fig. 14b). The advection (Fig. 14c) and vertical diffusion (Fig. 14d) terms at point N show similar patterns as those at point M, but there are also some
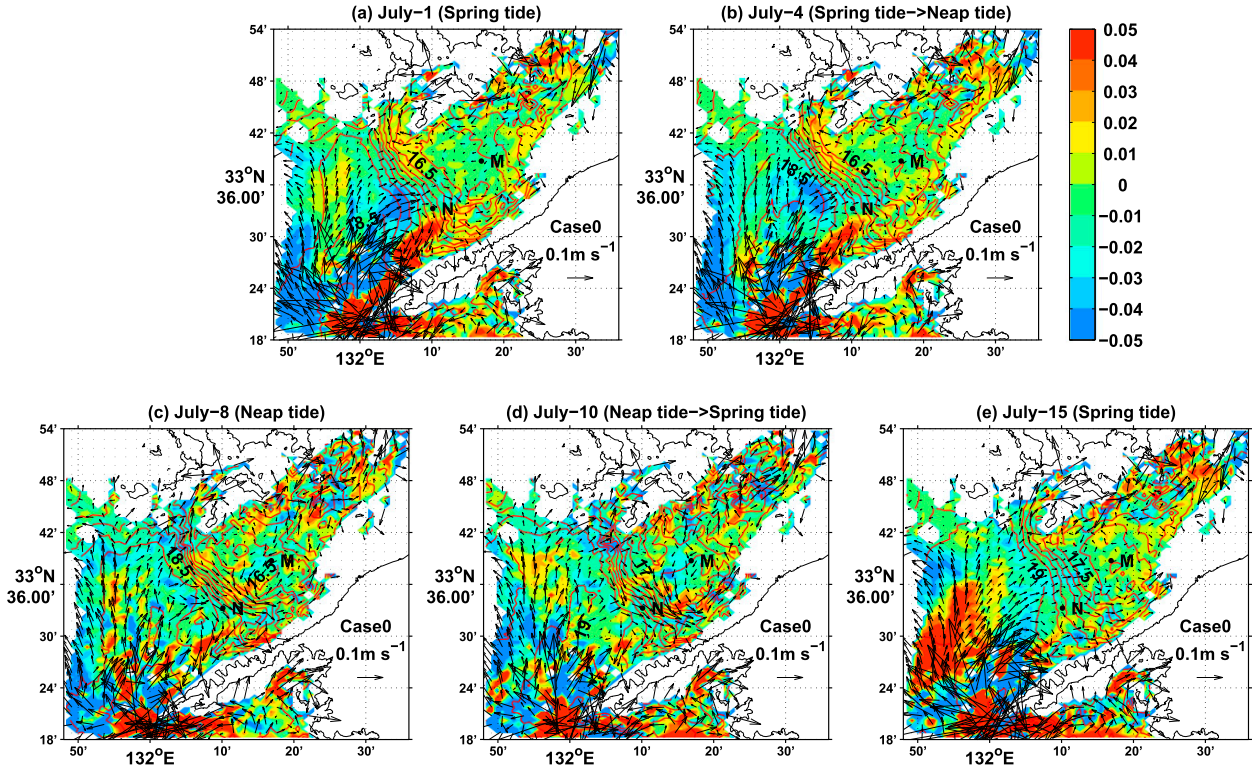
FIG. 15. Horizontal distribution of residual current (m s^{-1}; arrow), water temperature (°C; red line; CI = 0.25), and the component of residual current (m s^{-1}) flowing along the direction of the water temperature gradient [color; defined by Eq. (3)] at a depth of 45 m on 1, 4, 8, 10, and 15 Jul, covering a cycle from spring tide to the next spring tide for case 0.

notable differences. The advection term is much larger in the spring tide but becomes negative shortly after neap tide in the midlayer. This process induces the sum of advection and vertical diffusion to be much larger in spring tide but negative after neap tide. The change in sign of the advection term is likely caused by the change in the current field because the horizontal gradient of water temperature does not change its sign during the spring–neap–spring tidal cycle. As a result, the water temperature at point N increases faster from spring tide to neap tide but stops or even decreases after neap tide. Therefore, we attribute the different fortnightly variation of water temperature at points M and N to the advection term at point N.

To see what really occurs in the advection process, we calculated the residual current component UV in the direction along the gradient of water temperature using the following equation:

$$UV = \frac{\mathbf{V} \cdot \nabla T}{|\nabla T|} = \frac{u\dfrac{\partial T}{\partial x} + v\dfrac{\partial T}{\partial y}}{\sqrt{\left(\dfrac{\partial T}{\partial x}\right)^2 + \left(\dfrac{\partial T}{\partial y}\right)^2}}. \qquad (3)$$

Here, u and v are the eastward and northward components, respectively, of the residual current. If UV is positive, the residual current in the direction across the isotherms brings colder water to areas with high temperature and vice versa. From the horizontal distribution of UV (color overlay in Fig. 15) and residual currents (black arrows in Fig. 15) at a depth of 45 m, we can clearly see that there is a strong negative value area from the strait to the nada during the spring tide (1 July; Fig. 15a), which brings warmer water from the strait to outside of the BCW and increases the temperature there. This negative current is maintained on 4 July (Fig. 15b) but weakens or even becomes positive near the outside of the BCW during neap tide (8 July; Fig. 15c), indicating that it transfers colder water to the outside of the BCW from the inside. The UV stays positive after neap tide (10 July; Fig. 15d) but becomes negative again in spring tide (15 July; Fig. 15e). Consequently, the water temperature at N increases much faster from spring tide to neap tide and stops or even decreases after neap tide.

The residual current in case 1 (data not shown), that is, tide-induced residual current, flows from the strait to the nada and is stronger in spring tide than in neap tide.
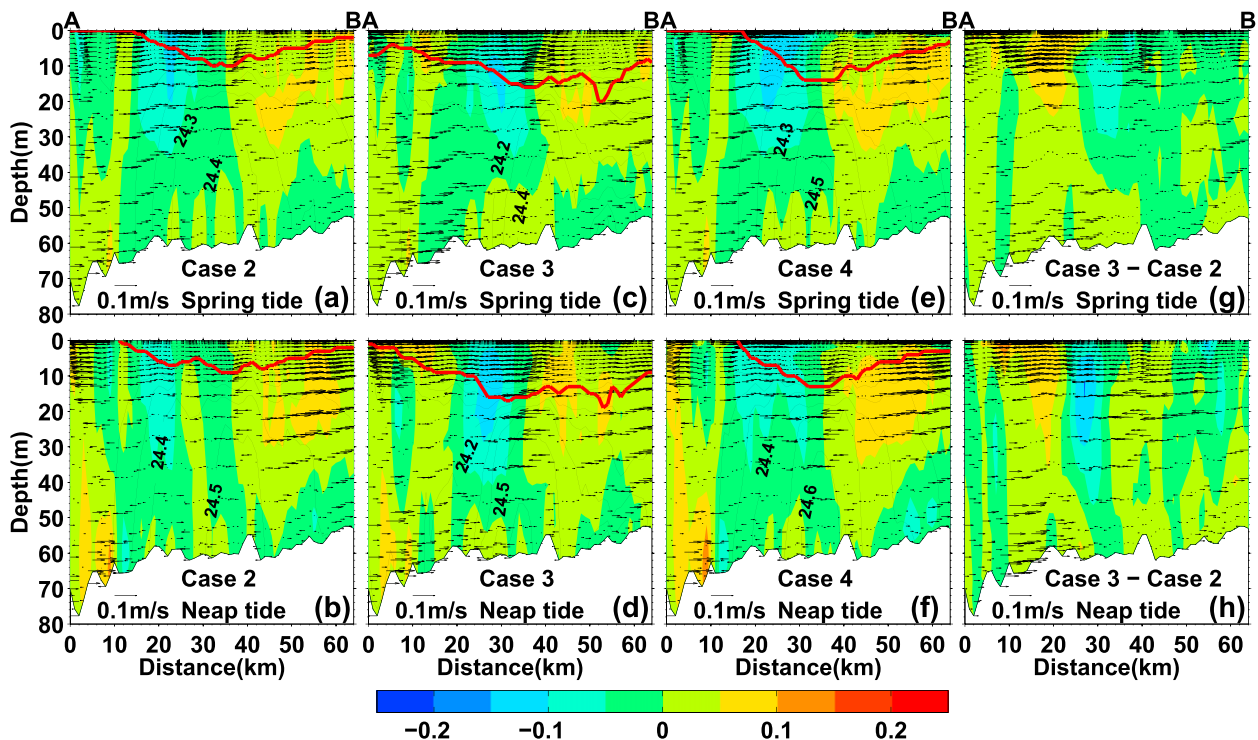
FIG. 16. Density (kg m^{-3}, black contours), residual current component normal to section AB (m s^{-1}; color), and residual current component parallel to section AB (m s^{-1}, arrows) for cases 2, 3, 4, and the difference between cases 2 and 3 (case 3 − case 2). Positive values for residual current component normal to section AB indicate inward current while negative values indicate outward current. Section AB is shown in Fig. 3. (top) Spring tide (red S in Fig. 7) and (bottom) neap tide (red N in Fig. 7). The thick red lines denote the position of the bottom boundary layer where the density is 0.5 kg m^{-3} less than that of bottom grid point. The density in cases 2 and 4 is calculated by setting salinity to 34.

Since it is strong only in the vicinity of the strait and cannot bring warm water from the strait to central area of the nada, this tide-induced residual current can only partly explain the strong and negative UV from the strait to the nada during the spring tide in case 0 (Fig. 15a). The addition of river discharge in case 3 nearly reproduced the strong and negative UV from the strait to the nada during the spring tide in case 0 (Fig. 15a), indicating that the bottom estuarine current also plays a role in carrying warm water from the strait to the central area of the nada. The addition of surface heating in case 2 and that of winds in case 4 has little effect on explaining the movement of warm water from the strait to the nada in spring tide. Therefore, advection heating by tide-induced residual current and the bottom estuarine current from the strait to the BCW are both important causative factors for the temperature increase outside of the BCW in spring tide.

A comparison of the residual current along section AB in cases 2–4 presents more information on the effects of the bottom residual current on the bottom thermal front (Fig. 16). The bottom residual current flows from the strait to the BCW in cases 2–4. This

current in case 3 is stronger in spring tide (Fig. 16c) than in neap tide (Fig. 16d). Such fortnightly variation is apparent in case 0 (Figs. 8e,f) but not apparent in cases 2 and 4. The difference between case 3 and case 2 shows a stronger bottom current in the area between the strait and the BCW (Figs. 16g,h), which must be a part of estuarine circulation over the entire basin because the difference in the boundary condition between two cases is the inclusion of river discharge in case 3 but exclusion of it in case 2. The fortnightly variation of the difference in residual currents between case 3 and case 2, which is stronger in neap tide than in spring tide, is also consistent with the well-known response of an estuarine circulation to the variation of tidal mixing with spring–neap tidal cycle, that is, the strong tidal mixing in spring tide induces a weak estuarine circulation and vice versa.

Although being the same tidally influenced sea, the bottom thermal front in the Irish Sea is strong in spring tide but weak in neap tide (Horsburgh and Hill 2003). This fortnightly variation is opposite to that in our study area. Holt and Proctor (2003) mentioned a current from the North Channel to the Irish Sea and its important role in bringing warm water to the BCW in the Irish Sea.
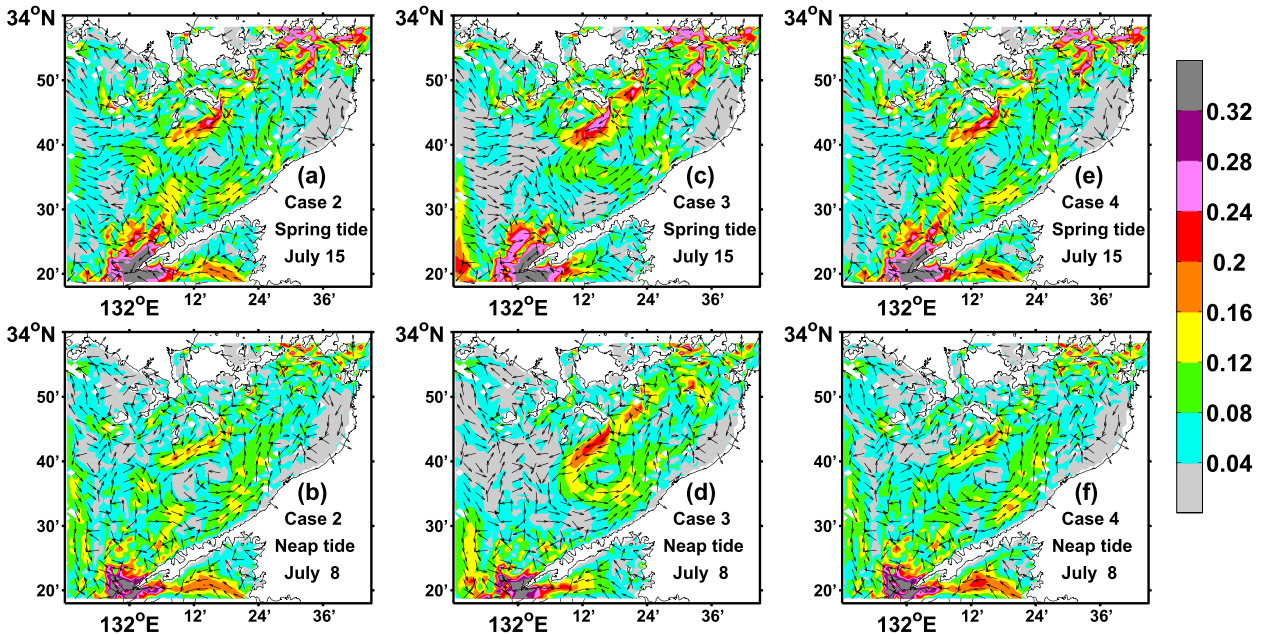
FIG. 17. Horizontal distribution of residual current at a depth of 10 m for cases 2–4. (top) Spring tide and (bottom) neap tide. The arrow shows the direction of current and the color overlay shows the magnitude of the current (m s^{-1}).

Since the current from the North Channel to the Irish Sea is influenced by shelf edge flow and wind (Xing and Davies 2001a), we suppose that its fortnightly variation is small and does not affect the fortnightly variation in the gradient of the bottom thermal front in the Irish Sea. Therefore, the gradient of the bottom thermal front in the Irish Sea is controlled mainly by the fortnightly variation of tidal mixing around the bottom thermal front, that is, the mixing area expands toward the stratification area in spring tide and retreats in neap tide; consequently, the gradient of the bottom thermal front in the Irish Sea is stronger in spring tide than in neap tide (Horsburgh and Hill 2003).

In our study area, not only tidal mixing but also bottom residual current in the direction of the cross front affect the gradient of the bottom thermal front. As demonstrated by our sensitivity experiments, the intensification of bottom residual currents between the strait and the BCW in case 3 induces a strong fortnightly variation in the gradient of the bottom thermal front. In some sense, the bottom residual currents between the strait and the BCW in our study area act as a "bridge" to bring the warm water from the strait to the outside of the BCW. The arrival of warm water at the outside of the BCW then intensifies the bottom thermal front. A comparison of case 2 and case 3 also supports this scenario. The bottom residual current in the cross-front direction between the strait and the BCW is stronger in case 3 than in case 2; the gradient of the bottom thermal

front is also stronger in case 3 than in case 2. Therefore, a stronger bottom residual current in the cross-front direction between the strait and the BCW induces a stronger bottom thermal front, as also demonstrated by the fortnightly variation of those in case 3. Therefore, the different behavior of ambient currents in the cross-front direction between our study area and the Irish Sea is the essential cause for the opposite fortnightly variation of bottom thermal front in two regions.

b. How does the bottom density gradient influence the surface cyclonic circulation during the spring–neap tidal cycle?

As described above, we set three cases (cases 2–4) to elucidate the variation of cyclonic circulation influenced by heating (case 2), river discharge (case 3), and wind (case 4). In case 2, even though the bottom temperature gradient is larger in neap tide than in spring tide, the horizontal distribution at the depth of 10 m (Figs. 17a,b) and the vertical distribution at the AB section (color; Figs. 16a,b) of the cyclonic circulation both showed circulation is larger in spring tide than in neap tide, which is the opposite of the pattern in case 0 (Figs. 8e,f; Figs. 9c, d). The addition of wind in case 4 (color; Figs. 16e,f, 17e,f) did not change the fortnightly variation in the surface cyclonic circulation in case 2. However, the addition of river discharge in case 3 (color; Figs. 16c,d, 17c,d) produces consistent fortnightly variation in the surface cyclonic circulation as observed for case 0.
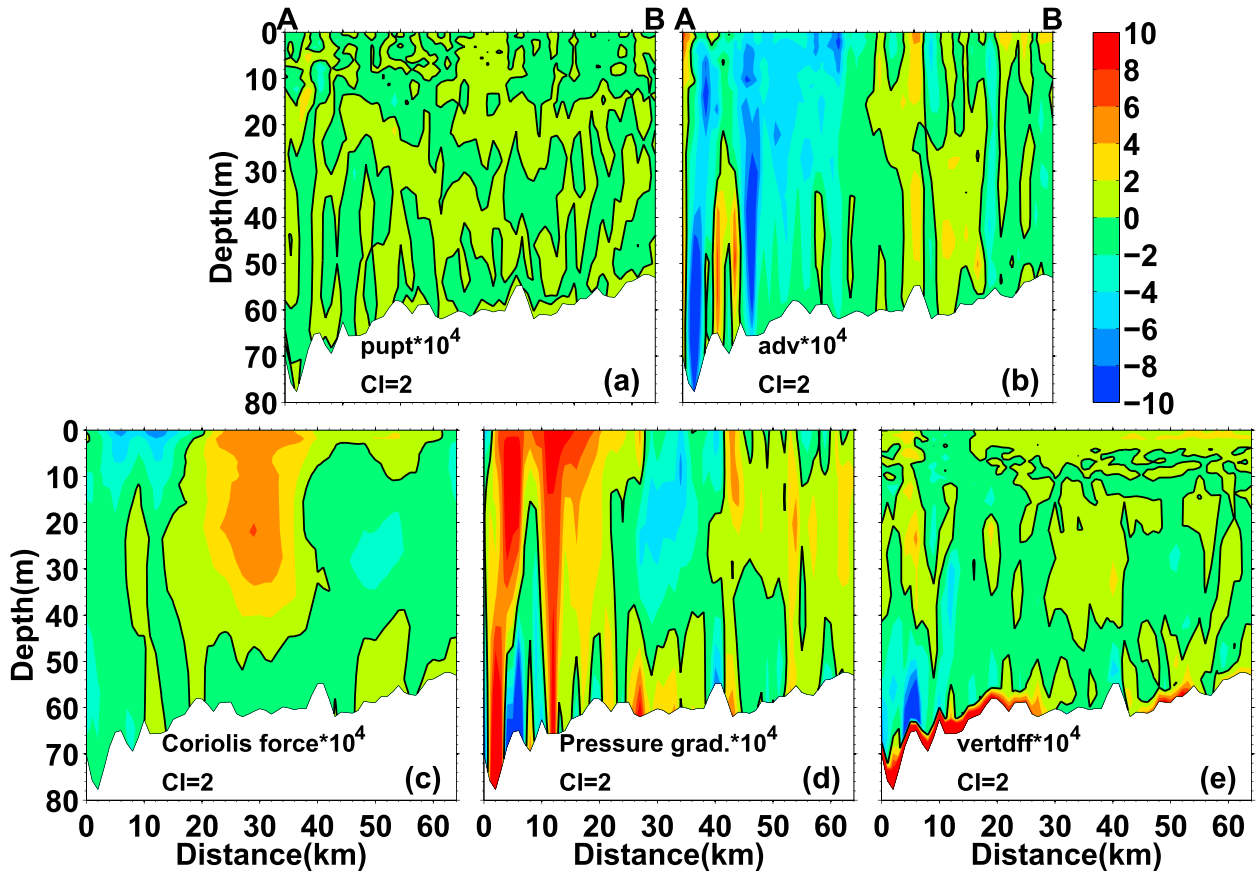
FIG. 18. Vertical distribution of the (a) time variable term, (b) advection term, (c) Coriolis force, (d) pressure gradient, and (e) vertical viscosity term in the momentum equation in the direction along section AB on 15 July (spring tide) for case 0 (CI = 2) (All values m^2 s^{-2}).

To understand dynamical causes for the different fortnightly variations in the surface cyclonic circulation in cases 0, 2, 3, and 4, we calculated the terms of the momentum equation [Eq. (4)] in the direction along the AB section in case 0 and applied the tide killer filter to every term to obtain tide-averaged results (Fig. 18):

$$\frac{\overline{\partial DU}}{\partial t} + \overline{adv} + \overline{cor} + \overline{pre} + \overline{ver\_vis} + \overline{F_x} = 0. \quad (4)$$

Here, D is water depth, U is the velocity component along the AB section, adv is the advection term, cor is the Coriolis forcing term, pre is the pressure gradient term, ver_vis is the vertical eddy viscosity term, and F_x is the horizontal eddy viscosity term. The overbar above each term is the tide filter.

Along section AB, the major momentum balance near the strait (0–15 km) is between the advection term (Fig. 18b) and the pressure gradient term (Fig. 18d), from which we can infer that a tide-induced residual current dominates in this area. In the area from 15 to

55 km, the major momentum balance is between the Coriolis force (Fig. 18c) and the pressure gradient force (Fig. 18d), from which we can infer that the cyclonic circulation above the BCW is a geostrophic current.

Based on the thermal-wind equation (Gill 1982) and assuming zero velocity at the sea bottom, we calculate the geostrophic current normal to section AB using the modeled density field (Fig. 19). The result showed a cyclonic circulation pattern from surface to subsurface, which is stronger in neap tide than in spring tide in case 0 and case 3 but is weaker in neap tide than in spring tide in case 2 and case 4 (Fig. 19). Since all of these features are similar to the residual currents calculated by the numerical model (Figs. 8e,f, 16), the geostrophic balance likely works well to explain the dynamics of the cyclonic circulation above the BCW.

Here, we consider the fortnightly variation of the cyclonic circulation above the BCW from the perspective of geostrophic balance. The velocity $V(z) = -g/(\rho f) \int_{-h}^{z} (\partial \rho)/(\partial x)\, dz$, based on the thermal-wind equation, is not only related to the horizontal density gradient $\partial \rho / \partial x$, but also depends on the
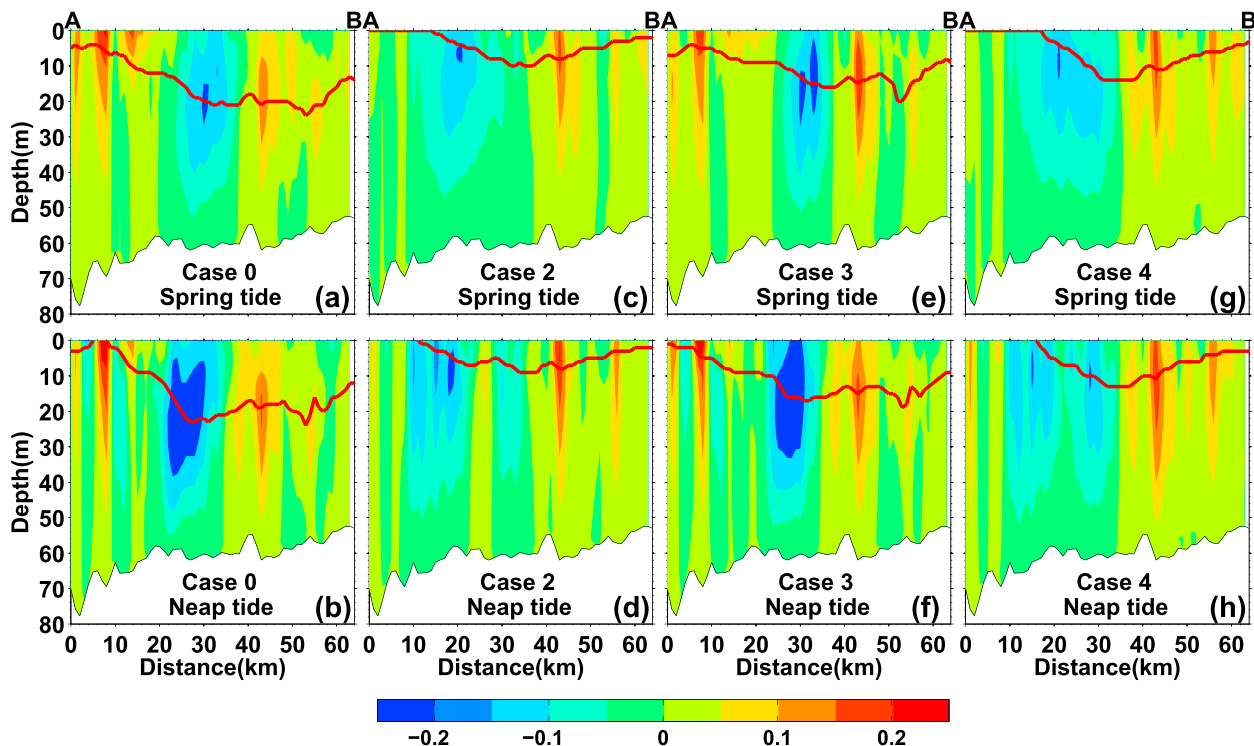
FIG. 19. Vertical distribution of calculated geostrophic current (m s^{-1}) from thermal-wind equation by using modeled density at section AB in Iyo-nada for case 0 and cases 2, 3, and 4 in (top) spring tide and (bottom) neap tide.

thickness of the BBL, where the horizontal density gradient is present. From Figs. 8e and 8f and Fig. 16, we can see that the BBL is thicker in spring tide than in neap tide in all cases. The observed BBL (Figs. 5e,f) is thicker in spring tide than in neap tide and is much more pronounced for station 3. This verifies that the modeled BBL is thicker in spring tide than in neap tide.

The effect of BBL thickness on the cyclonic circulation above the BCW is different in all of the cases. In cases 0 and 3, the BBL is generally thin (Fig. 10b), and the bottom density gradient and its fortnightly variation are generally large (Fig. 10a). Therefore, the cyclonic circulation above the BCW follows the fortnightly variation in the bottom density gradient, being strong in neap tide but weak in spring tide. In cases 2 and 4, however, the BBL is generally thick (Fig. 10b), and the bottom density gradient and its fortnightly variation are generally small (Fig. 10a). Therefore, the cyclonic circulation above the BCW follows the fortnightly variations in the BBL thickness, being strong in spring tide but weak in neap tide.

5. Conclusions

The results based on observational data and modeling both show that the bottom temperature gradient in

spring tide is smaller than that in neap tide in Iyo-nada of the Seto Inland Sea in July, which is different from the pattern observed in the Irish Sea where the bottom front gradient is larger in spring tide than in neap tide. The main mechanism causing such a different pattern in Iyo-nada and the Irish Sea is likely to be the horizontal advection of heat by the residual currents in Iyo-nada.

The temperature in the center of the BCW in Iyo-nada increased at almost the same rate during the spring–neap–spring tidal cycle, while that outside of the BCW increased sharply from spring tide to neap tide, decreased shortly after neap tide, and then increased again for the next spring tide. The sharp increase in temperature during spring tide was induced by the cross-front bottom residual current, bringing warmer water from the strait. This cross-front current is actually a combination of tide-induced residual current and the bottom estuarine current from the strait to the nada, which finally induced the larger temperature difference, that is, the larger temperature gradient in neap tide than in spring tide. Therefore, the difference between the Iyo-nada and the Irish Sea is that the bottom front gradient should be explained by the differing horizontal water advection and vertical mixing. In the Iyo-nada, both vertical mixing and horizontal advection are important in determining the bottom temperature gradient

during spring–neap tidal cycles. In the Irish Sea, vertical mixing is the major factor in determining the bottom temperature gradient during the spring–neap tidal cycle.

The BBL in Iyo-nada in summer is thicker in spring tide than in neap tide in both observational data and modeling results because the larger tidal current generates a larger vertical diffusion coefficient and thus forms a thicker BBL in spring tide.

The cyclonic circulation above the BCW is mainly in geostrophic balance. When considering the effect of tide, surface heating, and wind, the bottom density gradient changes little during the spring–neap tidal cycle, and the effect of BBL thickness on the cyclonic circulation is larger than that of the bottom density gradient; thus, the cyclonic circulation is stronger in spring tide than in neap tide. However, after adding the influence of river discharge, the bottom density gradient changes greatly during the spring–neap tidal cycle; meanwhile, the BBL becomes thin because of the intensification of stratification by river runoff. Consequently, the effect of the bottom density gradient on circulation becomes large, inducing greater circulation in neap tide than in spring tide. In the Irish Sea, both the bottom temperature gradient and the BBL thickness are larger in spring tide than in neap tide (Horsburgh and Hill 2003); therefore, cyclonic circulation is larger in spring tide than in neap tide.

REFERENCES

Blumberg, A. F., and G. L. Mellor, 1987: A description of a three dimensional coastal ocean circulation model. *Three-Dimensional Coastal Ocean Models, Coastal Estuarine Sci. Monogr.*, Vol. 4, Amer. Geophys. Union, 1–16, doi:10.1029/CO004p0001.

Brown, J., A. E. Hill, L. Fernand, and K. J. Horsburgh, 1999: Observations of a seasonal jet-like circulation at the central North Sea cold pool margin. *Estuarine Coastal Shelf Sci.*, **48**, 343–355, doi:10.1006/ecss.1999.0426.

——, L. Carrillo, L. Fernand, K. J. Horsburgh, A. E. Hill, E. F. Young, and K. J. Medler, 2003: Observations of the physical structure and seasonal jet-like circulation of the Celtic Sea and St. George's Channel of the Irish Sea. *Cont. Shelf Res.*, **23**, 533–561, doi:10.1016/S0278-4343(03)00008-6.

Chang, P.-H., X. Guo, and H. Takeoka, 2009: A numerical study of the seasonal circulation in the Seto Inand Sea, Japan. *J. Oceanogr.*, **65**, 721–736, doi:10.1007/s10872-009-0062-4.

Davies, A. M., and J. Xing, 2006: Effect of topography and mixing parameterization upon the circulation in cold water domes. *J. Geophys. Res.*, **111**, C03018, doi:10.1029/2005JC003066.

Gill, A. E., 1982: *Atmosphere–Ocean Dynamics*. Academic Press, 662 pp.

Guo, X., A. Futamura, and H. Takeoka, 2004: Residual currents in a semi-enclosed bay of the Seto Inland Sea, Japan. *J. Geophys. Res.*, **109**, C12008, doi:10.1029/2003JC002203.

——, K. Harai, A. Kaneda, and H. Takeoka, 2013: Simulation of tidal currents and nonlinear tidal interactions in the Seto Inland Sea, Japan. *Rep. Res. Inst. Appl. Mech. Kyushu Univ.*, **145**, 43–52.

Hanawa, K., and H. Mitsudera, 1985: On daily average of oceanographic data (in Japanese). *Coastal Oceanogr. Bull.*, **23**, 79–87.

Hill, A. E., 1996: Spin down and the dynamics of dense pool gyres in shallow seas. *J. Mar. Res.*, **54**, 471–486, doi:10.1357/0022240963213538.

——, R. Durazo, and D. A. Smeed, 1994: Observations of a cyclonic gyre in the western Irish Sea. *Cont. Shelf Res.*, **14**, 479–490, doi:10.1016/0278-4343(94)90099-X.

——, J. Brown, and L. Fernand, 1997: The summer gyre in the western Irish Sea: Shelf sea paradigms and management implications. *Estuarine Coastal Shelf Sci.*, **44**, 83–95, doi:10.1016/S0272-7714(97)80010-8.

——, ——, ——, J. Holt, K. J. Horsburgh, R. Proctor, R. Raine, and W. R. Turrell, 2008: Thermohaline circulation of shallow tidal seas. *Geophys. Res. Lett.*, **35**, L11605, doi:10.1029/2008GL033459.

Holt, J. T., and R. Proctor, 2003: The role of advection in determining the temperature structure of the Irish Sea. *J. Phys. Oceanogr.*, **33**, 2288–2306, doi:10.1175/1520-0485(2003)033<2288:TROAID>2.0.CO;2.

Horsburgh, K. J., and A. E. Hill, 2003: A three-dimensional model of the density-driven circulation in the Irish Sea. *J. Phys. Oceanogr.*, **33**, 343–365, doi:10.1175/1520-0485(2003)033<0343:ATDMOD>2.0.CO;2.

——, ——, J. Brown, L. Fernand, R. W. Garvine, and M. M. P. Angelico, 2000: Seasonal evolution of the cold pool gyre in the western Irish Sea. *Prog. Oceanogr.*, **46**, 1–58, doi:10.1016/S0079-6611(99)00054-3.

Lie, H.-J., 1989: Tidal fronts in the southeastern Hwanghae (Yellow Sea). *Cont. Shelf Res.*, **9**, 527–546, doi:10.1016/0278-4343(89)90019-8.

Loder, J. W., and D. A. Greenberg, 1986: Predicted positions of tidal fronts in the Gulf of Maine region. *Cont. Shelf Res.*, **6**, 397–414, doi:10.1016/0278-4343(86)90080-4.

Luyten, P. J., J. E. Jones, and R. Proctor, 2003: A numerical study of the long- and short-term temperature variability and thermal circulation in the North Sea. *J. Phys. Oceanogr.*, **33**, 37–56, doi:10.1175/1520-0485(2003)033<0037:ANSOTL>2.0.CO;2.

Lwiza, K. M. M., D. G. Bowers, and J. H. Simpson, 1991: Residual and tidal flow at a tidal mixing front in the North Sea. *Cont. Shelf Res.*, **11**, 1379–1395, doi:10.1016/0278-4343(91)90041-4.

Mellor, G. L., 2003: Users guide for a three-dimensional, primitive equation, numerical ocean model (2003 version). Atmospheric and Oceanic Sciences Program, Princeton University Rep., 53 pp.

——, and T. Yamada, 1982: Development of a turbulence closure model for geophysical fluid problems. *Rev. Geophys.*, **20**, 851–875, doi:10.1029/RG020i004p00851.

Mountain, D. G., and M. H. Taylor, 1996: Fluorescence structure in the region of the tidal mixing front on the southern flank of Georges Bank. *Deep-Sea Res. II*, **43**, 1831–1853, doi:10.1016/S0967-0645(96)00054-9.

Ou, H. W., 1984: Geostrophic adjustment: A mechanism for frontogenesis. *J. Phys. Oceanogr.*, **14**, 994–1000, doi:10.1175/1520-0485(1984)014<0994:GAAMFF>2.0.CO;2.

Simpson, J. H., and J. R. Hunter, 1974: Fronts in the Irish Sea. *Nature*, **250**, 404–406, doi:10.1038/250404a0.

——, and D. Bowers, 1981: Models of stratification and frontal movement in shelf seas. *Deep-Sea Res.*, **28A**, 727–738, doi:10.1016/0198-0149(81)90132-1.

——, and J. Sharples, 1994: Does the Earth's rotation influence the location of the shelf sea fronts? *J. Geophys. Res.*, **99**, 3315–3319, doi:10.1029/93JC03281.

——, C. M. Allen, and N. C. G. Morris, 1978: Fronts in the continental shelf. *J. Geophys. Res.*, **83**, 4607–4614, doi:10.1029/JC083iC09p04607.

Smagorinsky, J. S., 1963: General circulation experiments with the primitive equations. I. The basic experiment. *Mon. Wea. Rev.*, **91**, 99–164, doi:10.1175/1520-0493(1963)091<0099:GCEWTP>2.3.CO;2.

Su, J. L., and D. J. Huang, 1995: On the current field associated with the Yellow Sea cold water mass. *Oceanol. Limnol. Sin.*, **26**, 1–7.

Sun, Y.-J., and A. Isobe, 2006: Numerical study of tidal front with varying sharpness in spring and neap tidal cycle. *J. Oceanogr.*, **62**, 801–810, doi:10.1007/s10872-006-0099-6.

Takeoka, H., 1985: Density stratification in the Seto Inland Sea. *Umi Sora*, **60**, 145–152.

——, 2002: Progress in Seto Inland Sea research. *J. Oceanogr.*, **58**, 93–107, doi:10.1023/A:1015828818202.

——, O. Matsuda, and T. Yamamoto, 1993: Processes causing the chlorophyll α maximum in the tidal front in Iyo-nada, Japan. *J. Oceanogr.*, **49**, 57–70, doi:10.1007/BF02234009.

Wang, D. P., D. Chen, and T. J. Sherwin, 1990: Coupling between mixing and advection in a shallow sea front. *Cont. Shelf Res.*, **10**, 123–136, doi:10.1016/0278-4343(90)90026-I.

Xing, J., and A. M. Davies, 2001a: The influence of shelf edge flows and wind upon the circulation on the Malin shelf and in the Irish Sea. *Cont. Shelf Res.*, **21**, 21–45, doi:10.1016/S0278-4343(00)00073-X.

——, and ——, 2001b: A three-dimensional baroclinic model of the Irish Sea: Formation of the thermal fronts and associated circulation. *J. Phys. Oceanogr.*, **31**, 94–114, doi:10.1175/1520-0485(2001)031<0094:ATDBMO>2.0.CO;2.

——, and ——, 2005: A model study of spin-down and circulation in a cold water dome. *Ocean Dyn.*, **55**, 199–212, doi:10.1007/s10236-005-0007-4.

Yamamoto, T., T. Hashimoto, H. Takeoka, T. Sugiyama, and O. Matsuda, 2000: Middle layer intrusion as an important factor supporting phytoplankton productivity at a tidal front in Iyo nada, the Seto Inland Sea, Japan. *J. Oceanogr.*, **56**, 131–139, doi:10.1023/A:1011126911262.

Yanagi, T., and H. Higuchi, 1981: Tide and tidal current in the Seto Inland Sea (in Japanese). *Proc. 28th Conf. on Coastal Engineering*, Tokyo, Japan, Japan Society of Civil Engineers, 555–558.

——, and H. Tamaru, 1990: Temporal and spatial variations in a tidal front. *Cont. Shelf Res.*, **10**, 615–627, doi:10.1016/0278-4343(90)90041-J.

Yuan, Y.-L., and Li, H.-Q., 1993: On the circulation structure and formation mechanism of the cold water mass of the Yellow Sea (I)—Zero-order solution and circulation structure. *Sci. China Chem.*, **36**, 1518–1528.